Inorganic Chemistry

Article

pubs.acs.org/IC

A Template-Free Solution Route for the Synthesis of Well-Formed One-Dimensional Zn_2GeO_4 Nanocrystals and Its Photocatalytic Behavior

Jun Liang,[†,‡] Yiqun Cao,[†] Huan Lin,[†] Zizhong Zhang,[†] Changcang Huang,[†] and Xuxu Wang*[,†]

[†]Research Institute of Photocatalysis, Fujian Provincial Key Laboratory of Photocatalysis—State Key Laboratory Breeding Base, Fuzhou University, Fujian 350002, People's Republic of China

[‡]College of Chemistry and Chemical Engineering, Ningxia University, Yinchuan 750021, People's Republic of China

Supporting Information

ABSTRACT: Well-defined Zn_2GeO_4 hexagonal nanorods and nanofibers with high aspect ratios have been readily realized in high yield via a simple and general hydrothermal synthesis method free of any surfactant or template. Field-emission scanning electron microscopy (FESEM), transmission electron microscopy (TEM), energy-dispersive X-ray spectrometry (EDX), powder X-ray diffraction (XRD), and ultraviolet-visible light diffuse reflectance spectroscopy (UV—vis DRS) revealed a unique hexagonal-prism-shaped one-dimensional (1-D) structure, surface features, anisotropic crystal growth, and crystal phase of Zn_2GeO_4. Detailed investigations indicated that the prismatic Zn_2GeO_4 nanocrystals are uniform single crystal with the longitudinal direction along the [001] and were dominated by (110) and ($\bar{1}\bar{1}0$) surfaces. The addition of increasing amounts of NaOH was found to facilitate the morphology transition from a hexagonal nanorod shape to a hexagonal fiber shape. As an important wide-band-gap photocatalyst, the products of regular Zn_2GeO_4 nanocrystals with a hexagonal 1-D structure exhibit superior photocatalytic activities for the photocatalytic decomposition of water—methanol solution to hydrogen under UV irradiation.

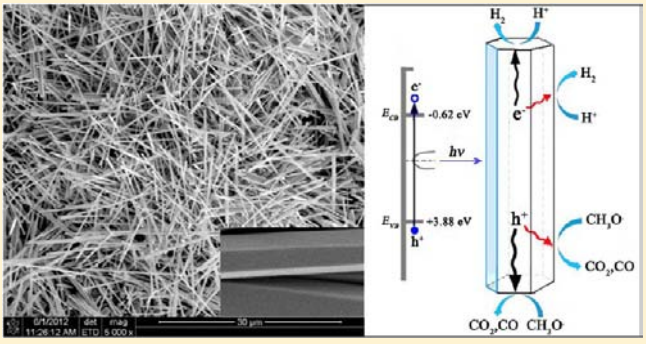

INTRODUCTION

The design and synthesis of one-dimensional (1-D) nanostructures with well-controlled morphology are important for uncovering their morphology-dependent properties and for achieving their practical applications in nanoscience and nanotechnology.[1−5] Two synthetic strategies have been generally employed for controlling the shape of these 1-D nanomaterials: (1) using a hard template to physically confine the size and shape of the growing nanoparticle, with the disadvantage of the method being that it relies extremely on templates; (2) using soft-templating route to control the growth direction and dimensions of nanoparticle, but the presence of the surfactants can easily result in the formation of byproducts.[6−8] Now it is realized that morphology control can be accomplished by manipulating the nuclei formation and subsequent crystal growth through optimizing the synthetic conditions without using any organic additives.[9]

In the recent decade, Zn_2GeO_4 with a 1-D structure has been largely reported as photoelectric device materials,[10] and as a photocatalyst for the splitting of water,[11,12] the reduction of CO_2,[13] and the degradation of organic pollutants.[14] Several routes have been developed to prepare the nanostructured materials. Huang et al. reported the synthesis of Zn_2GeO_4 nanorods via a cetyltrimethylammonium bromide (CTAB)-assisted hydrothermal method.[14] Yan and co-workers prepared Zn_2GeO_4 nanowires and their branched structures via a gold-catalyzed chemical vapor transport method.[15] Zhang et al. developed a microwave-assisted approach to prepare Zn_2GeO_4 nanorod bundles in a ternary ethylenediamine/PEG-400/water system.[16] Zou and co-workers reported the synthesis of single-crystalline nanoribbons of Zn_2GeO_4 in an ethylenediamine/water solvent system using a solvothermal route.[13] Yan et al. presented a low-temperature solution phase route under ambient pressure that does not need any additional process to obtain the Zn_2GeO_4 nanorods by the reaction of Na_2GeO_3 and $Zn(CH_3COO)_2$.[12] Recently, Yu et al. synthesized Zn_2GeO_4-ethylenediamine hybrid nanoribbons in the same ethylenediamine/water solvent system.[17] However, most synthetic processes require either a surfactant and an organic structure-directing agent or high temperature and high pressure. In addition, the introduced organic additives undoubtedly make synthetic procedure increased and lead to impurities in the final products. Therefore, a simple, rapid, and eco-friendly method for the synthesis of 1-D Zn_2GeO_4 materials is important for its applications.

Received: December 8, 2012
Published: May 28, 2013

   dx.doi.org/10.1021/ic302698z | Inorg. Chem. 2013, 52, 6916−6922

Herein, we develop a simple hydrothermal synthesis technique without any organic additives, and unexpectedly obtain hexagonal Zn_2GeO_4 nanorods and nanofibers with a high aspect ratio. The route is facile, controllable, and low-cost. The growth mechanism of the as-prepared samples was discussed. The obtained samples exhibit an excellent hydrogen-evolving activity by a water splitting reaction in the presence of methanol under UV-light irradiation.

EXPERIMENTAL SECTION

Synthesis of Zn_2GeO_4. All reagents used in the experiment were of analytical grade and used without further purification. A typical synthesis of hexagonal Zn_2GeO_4 nanorods was as follows: 0.4 g of NaOH (10 mmol) was dissolved into 20 mL of deionized water under stirring. Subsequently, 0.44 g of $Zn(CH_3COO)_2{\cdot}2H_2O$ (2.0 mmol) and 0.105 g of GeO_2 (1.0 mmol) then was added into the above solution. The mixture was stirred at room temperature to obtain a homogeneous solution, followed by transferring the solution into a 25-mL Teflon-lined stainless steel autoclave, sealed, and maintained at 473 K for 12 h. After slowly cooling to room temperature, the resulted solid was collected by centrifugation and washed with distilled water and absolute ethanol to remove any ionic residual material. The solid was dried in a vacuum oven at 343 K for 12 h. The hexagonal Zn_2GeO_4 nanofibers were obtained by adding 1.6 g of NaOH (40 mmol) to the hydrothermal reaction system under the same conditions as described above. The bulk Zn_2GeO_4 particles used for comparison was prepared by heating a stoichiometric mixture of GeO_2 and ZnO at 1473 K (ramp of 5 K/min) for 15 h.

Physicochemical Characterization. The phase purity and crystal structure of the sample were characterized by powder X-ray diffraction (XRD) on a Bruker D8 Advance X-ray diffractometer with Cu Kα radiation (λ = 1.54187 Å). More details about the chemical structure and morphology of the sample were obtained from selected-area electron diffraction (SAED) combined with high-resolution transmission electron microscopy studies (HRTEM, Tecnai Model G_2 F20 S-TWIN transmission electron microscope). The morphologies and sizes of the samples were examined by field-emission scanning electron microscopy (FESEM, Nova Model NanoSEM 230). The specific surface area of the samples was measured by nitrogen sorption at 77 K on a Micromeritics Model ASAP 2020 instrument and calculated using the Brunauer–Emmett–Teller (BET) method. The ultraviolet–visible light diffuse reflectance spectroscopy (UV-vis DRS) spectra were obtained by a Cary 500 Scan spectrophotometer using $BaSO_4$ as a reflectance standard.

Photocatalytic Performance. The photocatalytic hydrogen evolution reaction was performed in a closed gas-recirculation system equipped with a quartz reaction vessel with an inner irradiation. A small amount (0.1 g) of photocatalyst was dispersed in 155 mL of H_2O by magnetic stirring. Prior to the reaction, the system was evacuated by a mechanical pump and then filled with 101 kPa of high-purity N_2 (>99.99%). This process was repeated three times in order to completely remove O_2 from the system. After that, 5 mL of CH_3OH was introduced into the reactor with a syringe. The suspension was irradiated with a 125-W ultraviolet mercury lamp (Shanghai Yaming Lighting, Model GGZ-125). The temperature of the solution was controlled at room temperature by circulating water. The evolved hydrogen gas was circulated with a microdiaphragm gas pump in the system, and its amount was determined using an online gas chromatography (GC) device.

Photoelectrochemical Measurements. The measurements were conducted in a BAS Epsilon Electrochemical System with a conventional three-electrode cell. A platinum plate was used as the counter electrode, and Ag/AgCl electrode (3.0 mol L^{-1} KCl) was chosen as the reference electrode. Fifty milligrams (50 mg) of Zn_2GeO_4 powder was dispersed in 3 mL of ethanol in a centrifuge tube and sonicated for 30 min to obtain a slurry. The working electrode was prepared by spreading the slurry over an area of 0.25 cm^2 on an indium tin oxide (ITO) glass substrate. The film then was dried in air. The electrochemical measurement was carried out in a Na_2SO_4 (0.2 mol L^{-1}) electrolyte solution, which was purged with nitrogen gas for 2 h prior to the measurements. A 300 W xenon lamp (Beijin Changtuo, Model CHF-XM300) fitted by exposure to a UV was used as the light source.

RESULTS AND DISCUSSION

XRD patterns of the as-obtained hexagonal Zn_2GeO_4 nanorods and nanofibers were shown Figure 1. All the diffraction peaks of

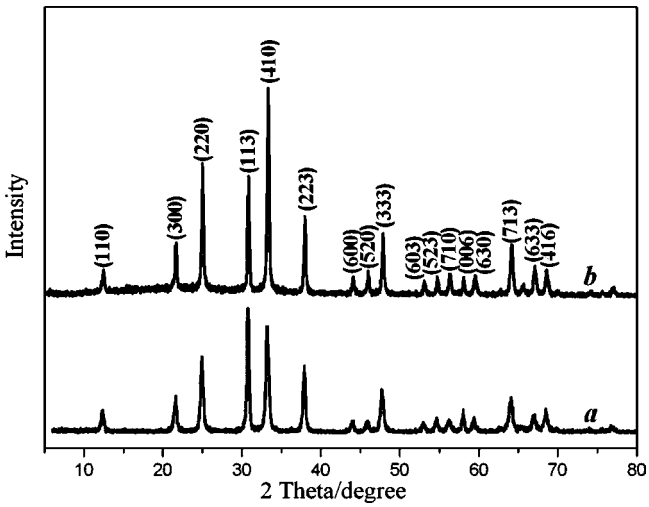

Figure 1. Typical XRD patterns of the as-prepared Zn_2GeO_4: (a) hexagonal nanorods and (b) hexagonal nanofibers.

the samples can be entirely indexed to a pure rhombohedral phase of Zn_2GeO_4 (JCPDS File Card No. 11-0687) with the lattice constants of $a = b$ = 14.231 Å, c = 9.530 Å, $\alpha = \beta = 90°$, and $\gamma = 120°$. No characteristic peaks for other types of impurities such as ZnO, GeO_2, etc., were observed. Thus, it can be confirmed that both products are pure rhombohedral Zn_2GeO_4 crystals.

Figure 2a shows a FESEM image of the hexagonal prismatic Zn_2GeO_4 nanorods prepared at 473 K with 0.4 g of NaOH. Very clearly, the sample is dominated by a morphology consisting of Zn_2GeO_4 with a rod-shaped 1-D nanostructure. According to the partially enlarged FESEM image shown in Figure 2b, each nanorod maintains its individual hexagonal rodlike shape (20–50 nm in diameter and between 200 nm and 1 μm in length), and the facets of hexagonal nanorods are identifiable. More details about the nanostructure and morphology of sample were done by TEM. It can be seen from Figures 2c and 2d that the sample has a hexagonal nanorod morphology, which is consistent with the FESEM observations.

Figures 3a and 3b show FESEM images of the hexagonal prismatic Zn_2GeO_4 nanofibers prepared at 473 K by using 1.6 g of NaOH. It can be seen that the sample is composed of a large quantity of randomly oriented and monodisperse nanofibers. Their lengths can reach up to 30 μm, and the diameters of the nanofibers are in a range of 50–700 nm. From partially enlarged FESEM images in Figures 3c and 3f, it is further clearly seen that these regular nanofibers own a hexagonal prism-shaped structure, and the facets of nanofibers are apparently distinguishable. It demonstrates well-defined shape of the Zn_2GeO_4 nanofiber. The morphological characteristics of sample are also supported by TEM observation (see Figures 3d and 3e). More importantly, the yield and purity of the

dx.doi.org/10.1021/ic302698z | Inorg. Chem. 2013, 52, 6916–6922

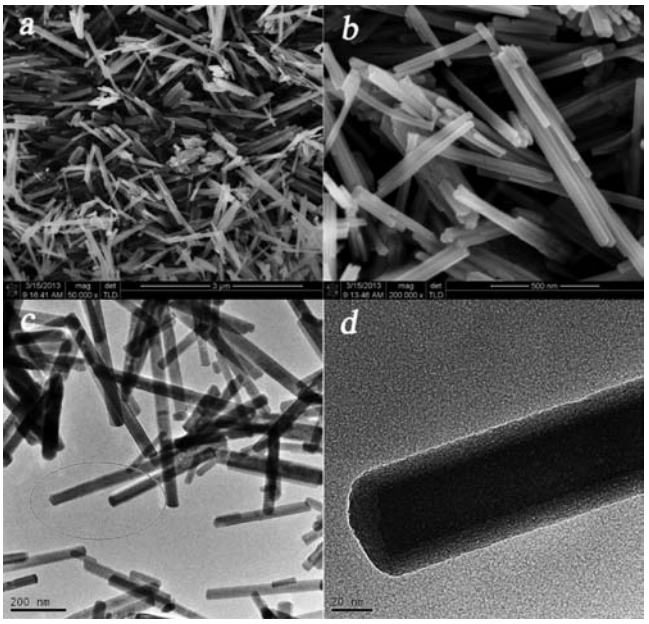

Figure 2. Typical (a) large-area and (b) partially enlarged FESEM images of the as-obtained Zn_2GeO_4 hexagonal nanorods. Typical (c) low-magnification and (d) high-magnification TEM images of the as-obtained Zn_2GeO_4 hexagonal nanorods.

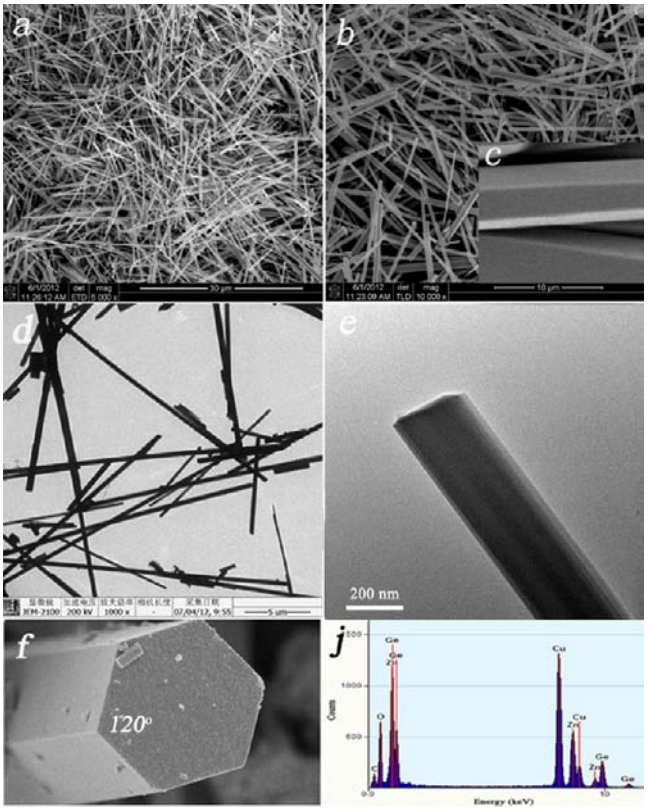

Figure 3. Typical (a) large-area and (b,c) partially enlarged FESEM images of the as-obtained Zn_2GeO_4 hexagonal nanofibers. Typical (d) low-magnification and (e) high-magnification TEM images of the Zn_2GeO_4 hexagonal nanofibers. (f) Enlarged FESEM image of the top of an individual hexagonal nanofiber. (j) Energy-dispersive X-ray spectroscopy (EDX) spectrum of the Zn_2GeO_4 hexagonal nanofibers.

hexagonal nanofibers are considerably high according to these images (see Figures 3a–d, as well as Figure S1 in the Supporting Information). Moreover, the EDX analysis (Figure 3j) shows that the nanofibers are composed of zinc, germanium, and oxygen and the Zn:Ge atomic ratio of ca. 2, which is consistent with the stoichiometric value for Zn_2GeO_4. The impurity peaks, which are assigned to Cu and C, are attributed to the supporting base used in the transmission electron microscopy (TEM) characterization.

To further obtain the detailed crystal structure of the prismatic Zn_2GeO_4 nanorods and nanofibers, HRTEM observations were obtained. Figures 4a and 4c show typical TEM images of the hexagonal Zn_2GeO_4 nanorods, and the corresponding HRTEM results, viewed from different positions, are displayed in Figures 4b and 4d, respectively. Figures 4e and 4f show typical TEM image of the hexagonal Zn_2GeO_4 nanofibers and its corresponding HRTEM image. Among these images, a uniform lattice fringe and a spot pattern of the selected-area electron diffraction (SAED) (see the inset in Figures 4a and 4e) verify that the two prismatic Zn_2GeO_4 samples show apparently single crystalline characteristics. The distance between the adjacent lattice fringes is 0.71 nm (Figure 4b), which can be assigned to the interplanar distance of the rhombohedral Zn_2GeO_4 (110) plane. Meanwhile, it is clearly observed that the lattice fringes are parallel to the growth direction of the rod. In Figure 4d, the lattice fringe of the (300) plane with an interplanar spacing of 0.41 nm is observed parallel to the nanorod direction. Another lattice fringe of the (003) plane with an interplanar spacing of 0.315 nm is observed, and it is vertical to the nanorod direction. According to the above structure information, we can conclude that the hexagonal Zn_2GeO_4 nanorods grew along the direction of the *c*-axis of the rhombohedral phenacite-type structure and can be enclosed by three equivalent (110), $(\bar{1}20)$, and $(2\bar{1}0)$ planes and three equivalent $(\bar{1}\bar{1}0)$, $(1\bar{2}0)$, and $(\bar{2}10)$ planes (see Figures 4g and 4h). More interestingly, the HRTEM result of the hexagonal Zn_2GeO_4 nanofiber (Figure 4f) is consistent with that of the hexagonal Zn_2GeO_4 nanorod (Figure 4d). In addition, further examinations also revealed that the lattice fringe of (110) with an interplanar spacing of 0.714 nm is observed in some tiny nanofibers, and it is parallel to the nanofiber direction (see Figure S3 in the Supporting Information). These characteristic results suggest that the resulting hexagonal Zn_2GeO_4 nanorods and Zn_2GeO_4 nanofibers are single crystals bounded by (110), $(\bar{1}20)$, $(2\bar{1}0)$, $(\bar{1}\bar{1}0)$, $(1\bar{2}0)$, and $(\bar{2}10)$ planes, and all of these planes belong to the family of the (110) plane.

In order to understand the formation process of the hexagonal-prism-shaped 1-D Zn_2GeO_4 nanocrystals and the possible growth mechanism, we observed the influence of the NaOH usage on the shape evolution by SEM, as shown in Figure 5. When the NaOH amount is 0.1 g, the resulting solid is mainly small-diameter Zn_2GeO_4 nanorods and a small number of prism-shaped Zn_2GeO_4 nanorods (Figure 5a). As the NaOH amount increases to 0.4 g, the product composition changes to hexagonal Zn_2GeO_4 nanorods (see Figures 5b and 2, as well as Figure S4 in the Supporting Information). Note that the size of the prismatic Zn_2GeO_4 nanorods increases with increasing NaOH usage (Figure 5c). However, by increasing the amount of the NaOH from 0.8 g to 1.6 g, a high yield of very uniform hexagonal Zn_2GeO_4 nanofibers is obtained (see Figures 5d and 3a, as well as Figure S1 in the Supporting Information). These results indicate that NaOH is responsible for the morphology transition from hexagonal nanorod shape to hexagonal nanofiber shape.

dx.doi.org/10.1021/ic302698z | *Inorg. Chem.* 2013, 52, 6916–6922

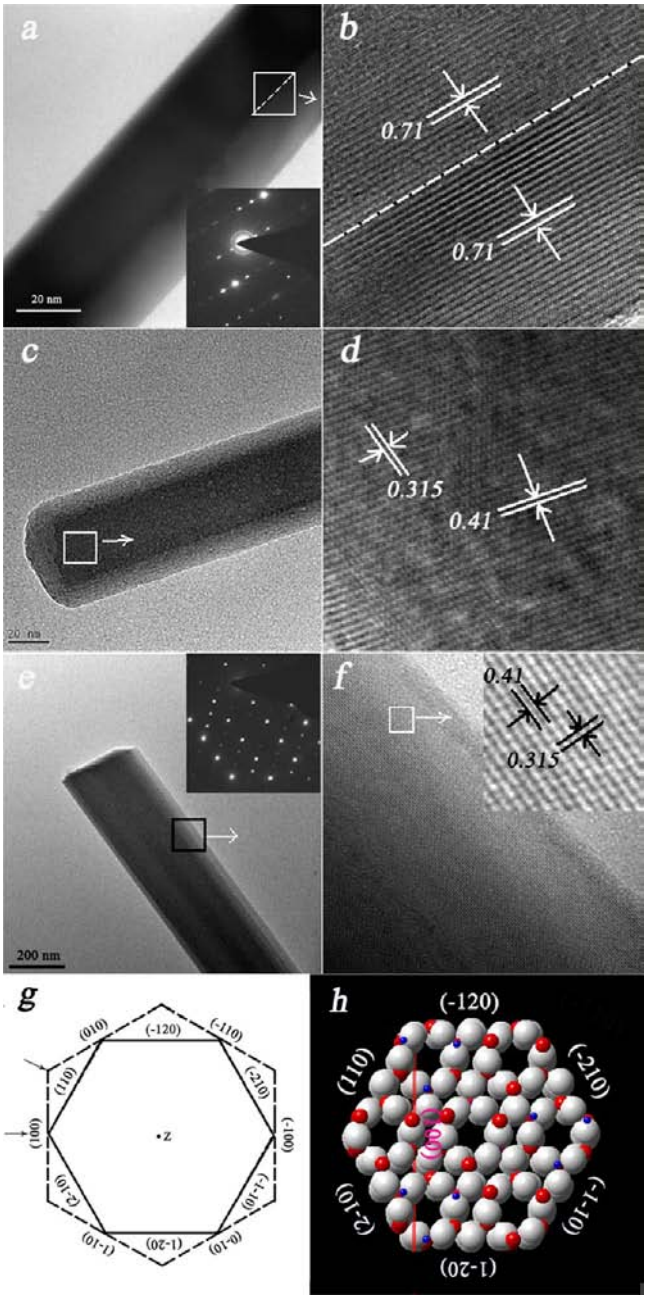

Figure 4. Typical (a,c) TEM and (b,d) HRTEM images of the Zn_2GeO_4 hexagonal nanorods viewed from different positions. Typical (e) TEM and (f) HRTEM images of the individual Zn_2GeO_4 hexagonal nanofiber. (g) Schematic illustration of the hexagonal prismatic Zn_2GeO_4 crystal partial planes and crystal orientation. (h) Space-filled structure model for the hexagonally prismatic Zn_2GeO_4 crystal with phenacite structure viewed along the *c*-axis (legend: red, Zn; white, O; blue, Ge). Insets in panels (a) and (e) are the corresponding SAED patterns.

In view of the HRTEM results reported above (Figure 4), on one hand, regarding to the crystal growth in the direction of the *c*-axis, this could be determined by the crystallographic feature of the phenacite structure. The Zn_2GeO_4 with phenacite structure is isostructural with the willemite Zn_2SiO_4.[18] The periodic bond chain theory predicts that the (100) and (110) planes are horizontal to the *c*-axis, which are considered to be energetically more stable than the (001) plane in crystallography.[12,18] Thus, the renascent nanocrystals of Zn_2GeO_4 would

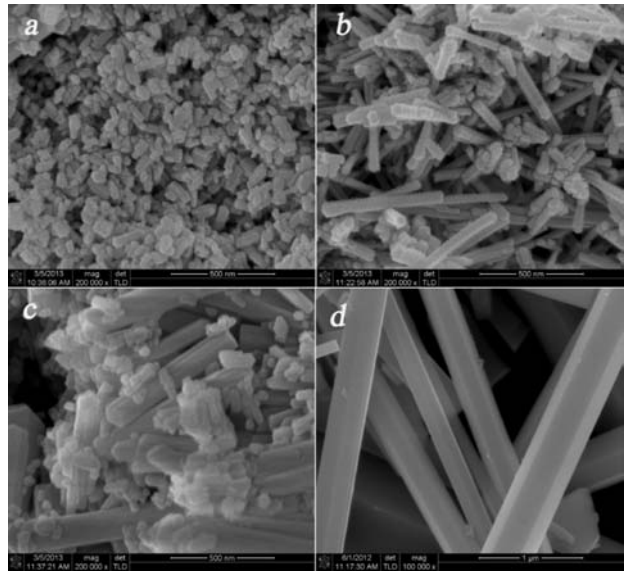

Figure 5. FESEM images of the products obtained at 200 °C with different NaOH concentrations: (a) 0.1 g, (b) 0.4 g, (c) 0.8 g, and (d) 1.6 g.

preferentially grow along the [001] direction. Zn_2GeO_4 has been also reported to form 1-D nanostructures growing along the [001] direction, including nanorods, nanoribbions, and more-complex structures composed of the ZnO_4 tetrahedra and GeO_4 tetrahedra basic units.[12,13,19] On the other hand, it is well-known that the anisotropy of crystal structure or the crystal surface reactivity is identified as the main driving force of the growth of the anisotropic structure. The phenacite Zn_2GeO_4 has internal hexagonal hollow tubes and directional polymerization axes of ZnO_4 and GeO_4 tetrahedra in the direction of the *c*-axis. Therefore, these Zn_2GeO_4 nanocrystals tend to grow along the [001] direction under present synthesis conditions, forming a hexagonal prism shape. A schematic illustration of the possible growth process of 1-D Zn_2GeO_4 nanocrystal is shown in Scheme 1. Herein, our experimental

Scheme 1. (a) Preferential Growth along One Direction (*c*-axis) of a Seed Crystal Results in Hexagonal Zn_2GeO_4 Nanorods and Nanofibers, and (b) Space-Filled Structure Model for the Prism-Shaped Zn_2GeO_4 Nanofiber along the *c*-axis[a]

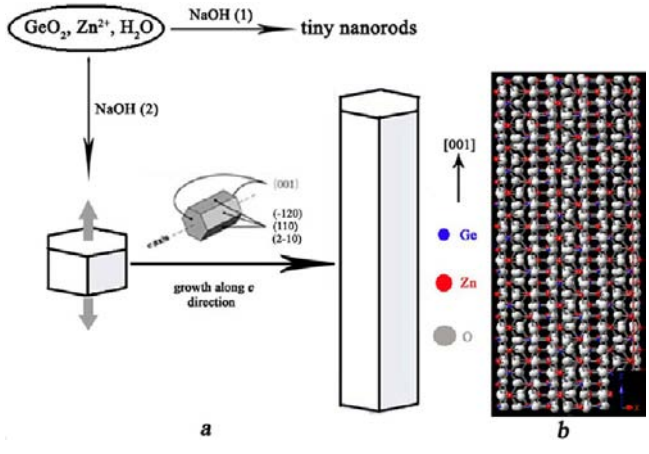

[a]Legend: blue, Ge; red, Zn; gray, O.

dx.doi.org/10.1021/ic302698z | Inorg. Chem. 2013, 52, 6916−6922

results indicate that the amount of NaOH adjusts the length:diameter ratio of the hexagonal prismatic Zn_2GeO_4 crystals and changes the morphology and size from a hexagonal nanorod shape to a hexagonal nanofiber shape. That is to say, NaOH, as a mineralizer, is vital for the morphological evolution of 1-D prism-shaped Zn_2GeO_4 nanocrystals. At any rate, the growth habits of the Zn_2GeO_4 crystal must be probed further.

The relationship between the structure and the optical properties has been investigated by UV-vis DRS and is shown in Figure 6. Under UV-light irradiation, electrons in the valence

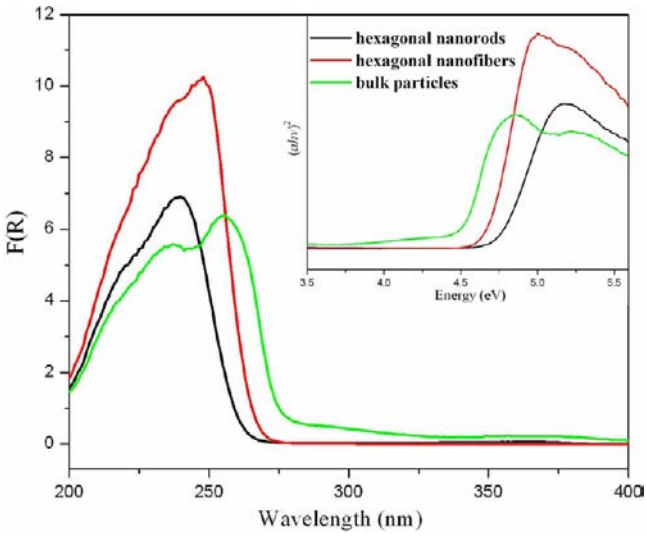

Figure 6. UV−visible light diffuse reflectance spectroscopy (UV-vis DRS) spectra of the bulk Zn_2GeO_4 particles, hexagonal Zn_2GeO_4 nanorods, and hexagonal Zn_2GeO_4 nanofibers. Inset shows the optical band gap energy (E_g) of the corresponding sample.

band (VB) absorb the photon energy and jump to the conduction band (CB), leaving holes in the VB. Light absorption is mainly determined by the band structure and dipole matrix elements. From Figure 6, it can be deduced that the bulk particles, prism-shaped nanorods, and nanofibers have band gaps of ca. 4.5, 4.67, and 4.64 eV, respectively, corresponding to optical absorption edges of ca. 275, 265, and 267 nm, respectively. The light absorption edges of hexagonal prismatic Zn_2GeO_4 samples exhibit a certain extent of blue shift, in comparison with that of bulk Zn_2GeO_4 particles, which can be explained by the size effect.[20] However, there is no significant difference in the absorption edges of the prismatic Zn_2GeO_4 samples.

The photoresponse time profiles of hexagonal prismatic Zn_2GeO_4 nanocrystals were investigated. For comparison, bulk Zn_2GeO_4 film electrode was also measured. Figure 7 displays the periodic photoresponses of the Zn_2GeO_4 samples obtained, which were switched between high- and low-conductivity states by turning the light source on and off five times. When the Zn_2GeO_4 samples were irradiated with UV light, a strong photocurrent response could be observed for the three samples that were coated on ITO glass plates. However, the hexagonal prismatic Zn_2GeO_4 nanocrystals show significant improvement in photocurrent, in comparison with bulk Zn_2GeO_4 particles. The result suggests that the unique nanostructure of prismatic Zn_2GeO_4 samples can lead to an enhanced photoresponse, indicating a new strategy of hexagonal 1-D Zn_2GeO_4 nanomaterials to effectively amplify the optoelectronic proper-

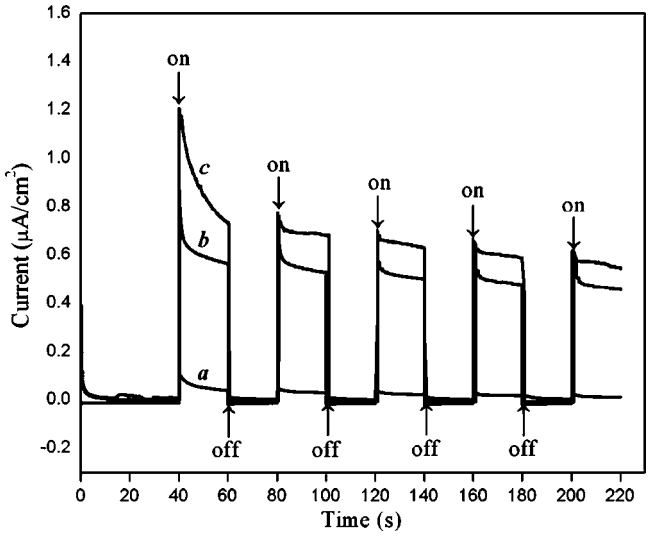

Figure 7. Periodic on/off photocurrent response of bulk Zn_2GeO_4 particles (trace a), hexagonal Zn_2GeO_4 nanorods (trace b), and hexagonal Zn_2GeO_4 nanofibers (trace c) under exposure to UV light.

ties of 1-D nanostructures. This provides further evidence that efficient photoinduced charge separation and transfer can occur on the hexagonal prismatic Zn_2GeO_4 samples.

Photocatalytic H_2 production from a methanol−water solution, as a model reaction, was used to evaluate the photocatalytic performance of the hexagonal-prism-shaped 1-D Zn_2GeO_4 nanocrystals under UV-light irradiation. The controlled blank reaction in the absence of any catalyst showed no H_2 formation. The photocatalytic activities were also compared with those of the P25 TiO_2 and bulk Zn_2GeO_4 particles. Figure 8A shows that the amount of H_2 evolved over each catalyst increased proportionally with reaction time, indicating that the photocatalytic reaction proceed steadily in each case, but all the Zn_2GeO_4 samples show higher H_2-producing activities than the P25 TiO_2. Among Zn_2GeO_4 samples, Zn_2GeO_4 samples with a 1-D nanostructure are superior, with regard to the activity to the bulk Zn_2GeO_4 particles. According to the slopes of these straight-line plots of hydrogen evolution amounts versus reaction time, the calculated gas evolution rate for various samples prepared by various synthesis methods is displayed in Figure 8B. The hexagonal Zn_2GeO_4 nanorods show the highest rate of H_2 evolution, and the evolution rate of hydrogen gas is 13.5 mL h^{-1} (0.6 mmol h^{-1}). The photocatalytic activity decreased in the order of hexagonal Zn_2GeO_4 nanorods > hexagonal Zn_2GeO_4 nanofibers > bulk Zn_2GeO_4 particles > P25 TiO_2 (Figure 8B).

Based on the preceding structural and optical characterizations, although the Zn_2GeO_4 samples possessed the same phase structure (see Figure 1, as well as Figure S5 in the Supporting Information) and similar photoadsorption efficiency (Figure 6), the hexagonal prismatic nanorods exhibited the best photocatalytic H_2-evolving activity. This may be mainly ascribed to the following three factors. First, it is well-known that the surface structure of photocatalysts play vital roles to their photocatalytic activities, because the photocatalytic reaction or photoelectron conversion takes place only when photoinduced electrons and holes are available on the surface. Some studies[21,22] have also demonstrated that the photocatalysts exposed with various reactive facets or directions have

dx.doi.org/10.1021/ic302698z | Inorg. Chem. 2013, 52, 6916−6922

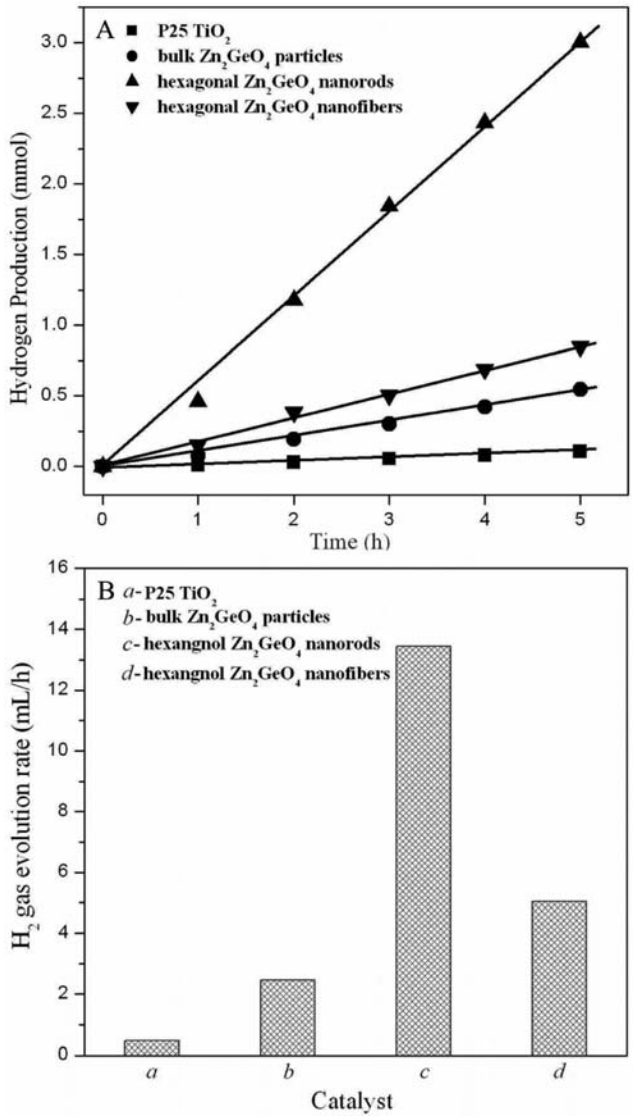

Figure 8. (A) Photocatalytic hydrogen evolution and (B) hydrogen evolution rate from an aqueous methanol solution over various photocatalysts under exposure to UV light. Catalyst amount, 0.1 g; H_2O volume, 155 mL; CH_3OH volume, 5 mL.

an important effect on the enhanced photocatalytic activities. In our cases, we believed that the enhanced photocatalytic activity on prismatic Zn_2GeO_4 crystals can be related to their surface structures in the present system. To further identify this, an auxiliary experiment was performed. When different amounts of NaOH were added to the hydrothermal reaction system, while other synthetic conditions were maintained constant (see Figure 5), the H_2-producing activities of the Zn_2GeO_4 samples obtained with different NaOH concentrations are shown in Figure 9. Among Zn_2GeO_4 samples, the BET surface area of the hexagonal Zn_2GeO_4 nanorods is 30.8 $m^2\ g^{-1}$, which is less than that of the Zn_2GeO_4 nanorods (33.2 $m^2\ g^{-1}$). However, the prismatic nanorods exhibited significantly higher rates of H_2 evolution than the Zn_2GeO_4 nanorods (see Figures 9a and 9b). The result indicates that the surface structure of prismatic Zn_2GeO_4 crystals can influence the photocatalytic activities of Zn_2GeO_4 samples. In view of above results analysis, the unique surface structure of hexagonal prismatic Zn_2GeO_4 nanocrystals may accelerate efficient separation and transfer of photoinduced

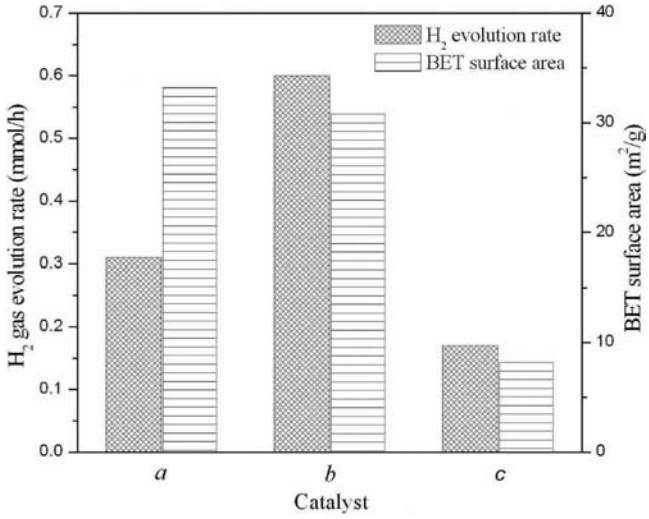

Figure 9. Photocatalytic hydrogen evolution rate and BET surface area of (a) Zn_2GeO_4 nanorods, (b) hexagonal Zn_2GeO_4 nanorods, and (c) hexagonal Zn_2GeO_4 nanofibers synthesized at 200 °C from 0.1 g, 0.4 g, and 1.6 g of NaOH, respectively. Catalyst amount, 0.1 g; H_2O volume, 155 mL; CH_3OH volume, 5 mL.

charges and therefore retard the recombination of photogenerated electron−hole pairs. However, we also observed that H_2-producing rate of hexagonal Zn_2GeO_4 nanofibers is less than that of the Zn_2GeO_4 nanorods (see Figures 9a and 9c). This means that the enhanced photocatalytic activity is not dominated completely by the surface structure of prismatic Zn_2GeO_4 nanocrystals. However, it is therefore noteworthy that the specific surface area of the Zn_2GeO_4 nanorods (33.2 $m^2\ g^{-1}$) is much greater than that of the Zn_2GeO_4 nanofibers (8.2 $m^2\ g^{-1}$). Meanwhile, with regard to hexagonal prismatic Zn_2GeO_4 samples (Figure 9b and 9c), the H_2-producing rates of similarly nanostructured Zn_2GeO_4 samples are decreased as their specific surface area decreases. These results clearly show that the enhanced photocatalytic activities of Zn_2GeO_4 samples are also dependent on the specific surface area. This might be because high-specific-surface-area Zn_2GeO_4 samples can provide more reaction sites and, therefore, improve their photocatalytic activities. In addition, a 1-D nanostructure with a high aspect ratio is favorable for photogenerated carrier transport and transfer by ballistic charge transport along the single-crystal Zn_2GeO_4 nanorod direction. Some studies[22,23] also suggested that ballistic charge transport along the direction of 1-D nanocrystals should be much more efficient than diffusive transport in the powdered materials. This was also demonstrated through the short-circuit photocurrent response results reported above (see Figure 7).

On the basis of the above analysis, although we do not ultimately make the decisive factor of H_2 production clear and also cannot provide direct evidence to understand the exact nature of the differences in photocatalytic activities of different Zn_2GeO_4 samples, our work suggests that photocatalytic activity can be improved because of the high specific surface area, beneficial surface structures, and 1-D nanostructure with high aspect ratios in water splitting reaction in the presence of methanol under UV-light irradiation.

■ CONCLUSION

In summary, high-quality one-dimensional (1-D) Zn_2GeO_4 nanorods and nanofibers with hexagonal-prismatic structure

dx.doi.org/10.1021/ic302698z | Inorg. Chem. 2013, 52, 6916−6922

were successfully synthesized via a simple template-free hydrothermal synthetic route, using $Zn(OAc)_2 \cdot 2H_2O$ and GeO_2 in alkaline aqueous solution. The experimental results demonstrated that the hexagonal prism-shaped Zn_2GeO_4 nanocrystals were dominated by (110), $(2\bar{1}0)$, $(1\bar{2}0)$, $(\bar{1}10)$, $(\bar{2}10)$, and $(\bar{1}20)$ planes. The detailed growth mechanism of prismatic Zn_2GeO_4 nanocrystals was suggested. The photocatalytic investigations show that well-formed 1-D Zn_2GeO_4 nanorods and nanofibers exhibit excellent photocatalytic activities in the photocatalytic decomposition of a water−methanol solution to hydrogen under UV irradiation. Our results indicated that the geometric shape of the Zn_2GeO_4 nanocrystal may be an important factor in the catalyst design, besides the specific surface area. Furthermore, this facile, controllable, low-cost, and environmentally friendly synthesis method does not require any seed crystals, templates, or organic additives. Therefore, this successful synthesis strategy is expected to be utilized in the large-scale preparation of single-crystalline Zn_2GeO_4 hexagonal 1-D nanomaterials.

■ ASSOCIATED CONTENT

Ⓢ Supporting Information

SEM images, TEM images, XRD pattern, and HRTEM results. This material is available free of charge via the Internet at http://pubs.acs.org.

■ AUTHOR INFORMATION

Corresponding Author

*E-mail: xwang@fzu.edu.cn.

Notes

The authors declare no competing financial interest.

■ ACKNOWLEDGMENTS

This work was financially supported by the NSFC (Grant Nos. 21173044, 21203029, and 21003021), and the National Basic Research Program of China (973 Program, No. 2012CB722607).

■ REFERENCES

(1) Zhao, Z. G.; Miyauchi, M. *Angew. Chem., Int. Ed.* **2008**, *47*, 7051−7055.
(2) Liu, A. H.; Wei, M. D.; Honma, I.; Zhou, H. S. *Adv. Funct. Mater.* **2006**, *16*, 371−376.
(3) Shankar, K.; Bandara, J.; Paulose, M.; Wietasch, H.; Varghese, O. K.; Mor, G. K.; LaTempa, T. J.; Thelakkat, M.; Grimes, C. A. *Nano Lett.* **2008**, *8*, 1654−1659.
(4) Hosono, E.; Kudo, T.; Honma, I.; Matsuda, H.; Zhou, H. S. *Nano Lett.* **2009**, *9*, 1045−1051.
(5) Song, S. P.; Qin, Y.; He, Y.; Huang, Q.; Fan, C. H.; Chen, H. Y. *Chem. Soc. Rev.* **2010**, *39*, 4234−4243.
(6) Cao, M. H.; Liu, T. F.; Gao, S.; Sun, G. B.; Wu, X. C.; Hu, W.; Wang, Z. L. *Angew. Chem., Int. Ed.* **2006**, *47*, 4197−74201.
(7) Yao, W. T.; Yu, S. H. *Adv. Funct. Mater.* **2008**, *18*, 3357−3366.
(8) Hagrman, Pamela J.; Hagrman, D.; Zubieta, J. *Angew. Chem., Int. Ed.* **1999**, *38*, 2638−2684.
(9) Shi, W. D.; Wang, C.; Wang, H. H.; Zhang, H. J. *Cryst. Growth Des.* **2006**, *6*, 915−918.
(10) Yan, C.; Lee, P. S. *J. Phys. Chem. C* **2010**, *114*, 265−268.
(11) Sato, J.; Kobayashi, H.; Ikarashi, K.; Saito, N.; Nishiyama, H.; Inoue, Y. *J. Phys. Chem. B* **2004**, *108*, 4369−4375.
(12) Yan, S. C.; Wan, L. J.; Li, Z. S.; Zou, Z. G. *Chem. Commun.* **2011**, *47*, 5632−5634.
(13) Liu, Q.; Zhou, Y.; Kou, J. H.; Chen, X. Y.; Tian, Z. P.; Gao, J.; Yan, S. C.; Zou, Z. G. *J. Am. Chem. Soc.* **2010**, *132*, 14385−14387.
(14) Huang, J.; Ding, K.; Hou, Y.; Wang, X. X.; Fu, X. Z. *ChemSusChem* **2008**, *1*, 1011−1019.
(15) Yan, C. Y.; Lee, P. S. *J. Phys. Chem. C* **2009**, *113*, 14135−14139.
(16) Zhang, L.; Cao, X. F.; Ma, Y. L.; Chen, X. T.; Xue, Z. L. *CrystEngComm* **2010**, *12*, 3201−3206.
(17) Yu, L.; Zou, R. J.; Zhang, Z. Y.; Song, G. S.; Chen, Z. G.; Yang, J. M.; Hu, J. Q. *Chem. Commun.* **2011**, *47*, 10719−10721.
(18) Sun, C.; Kuan, F. J.; Kao, F. J.; Wang, Y. M.; Chen, C. J.; Chang, C. C.; Shen, P. *Mater. Sci. Eng., A* **2004**, *379*, 327−333.
(19) Liu, Q.; Zhou, Y.; Tian, Z. P.; Chen, X. Y.; Gao, J.; Zou, Z. G. *J. Mater. Chem.* **2012**, *22*, 2033−2038.
(20) Zhang, Y.; Duan, F.; Wu, J.; Liu, L.; Chen, M. Q.; Xie, Y. *J. Mol. Catal. A: Chem.* **2009**, *303*, 9−14.
(21) Kato, H.; Asakura, K.; Kudo, A. *J. Am. Chem. Soc.* **2003**, *125*, 3082−3086.
(22) Wu, N. Q.; Wang, J.; Tafen, D.; Wang, H.; Zheng, J. G.; Lewis, J. P.; Liu, X. G.; Leonard, S. S.; Manivannan, A. *J. Am. Chem. Soc.* **2010**, *132*, 6679−6684.
(23) Wang, D. F.; Pierre, A.; Kibria, M. G.; Cui, K.; Paradis, S.; Hakima, A.-R.; Mi, Z. *Nano Lett.* **2011**, *11*, 2353−2357.